SSRG International Journal of Electrical and Electronics Engineering
ISSN: 2348-8379/ https://doi.org/10.14445/23488379/IJEEE-V13I7P103

Volume 13 Issue 7, 50-69, July 2026

Original Article

Experimental Investigation of a SRR Unit-Cell Driven Multiband Bandpass Filter using a T Shaped DGS for 5G FR_1 Bands n77, n78, and n79 with Enhanced Stopband Suppression

Gauravkumar R. Asari[1], Priti J. Muliya[2]

[1]*Department of Electronics and Communication Engineering, Vishwakarma Government Engineering College, Chandkheda, Ahmedabad, Gujarat, India.*
[2]*Department of Electronics and Communication Engineering, L.D. College of Engineering, Ahmedabad, Gujarat, India.*

[1]*Corresponding Author : grsasari@vgecg.ac.in*

Received: 13 May 2026 Revised: 13 June 2026 Accepted: 19 June 2026 Published: 27 July 2026

Abstract *- This paper presents the design, simulation, fabrication, and measurement of a novel multiband microstrip based Bandpass Filter (BPF) for 5G FR_1 mid-band operation intertwining a cascaded Split Ring Resonator (SRR) unit-cell array on the top metal layer with a T-shaped Defected Ground Structure (DGS) etched into the ground covering n77 (3.3-4.2 GHz), n78 (3.3-3.8 GHz), and n79 (4.4-5.0 GHz) frequency bands. The SRR array enables regulated resonant loading and allows for multiband transmission and better skirt selectivity. The DGS, on the other hand, disturbs the return current path to generate transmission zeros and suppress the high-frequency spurious responses for maximizing the stopband attenuation. First, the retrieval of effective constitutive parameters of the proposed unit cell is performed in the goal of illustrating the metamaterial behavior. Great focus is put on permeability that demonstrates magnetic-resonance behavior at the design frequency of 4.7GHz. The entire filter is designed, developed and optimized in Ansys HFSS, fabricated on a FR-4 substrate and characterized using an Anritsu MS46122B Vector Network Analyzer (VNA). The measured return loss (S_{11}) and insertion loss (S_{21}) responses agree well with the simulated results and show reliable mid-band transmission within the criteria of 5G FR_1 and maximum stopband suppression. The proposed SRR-DGS-based BPF provides a promising way for a compact design of multiband 5G front-end filters, low-profile and easy to fabricate.*

Keywords *- Split Ring Resonator (SRR), Defected Ground Structure (DGS), n77/n78/n79, HFSS, 5G FR_1, VNA.*

1. Introduction

The advent of 5G New Radio (NR) has imposed stringent performance constraints on the RF front-end subsystems, especially with respect to the filters straddled between crowded spectrum bands occupied by aggregated carriers and strict emission masks. In both the transmission and reception chains, BPFs are a must because they define the channel selectivity, as well as filter out adjacent-band interference and protect sensitive Low Noise Amplifiers (LNAs) from high out-of-band blockers. The ideal answer for the next wave of discrimination standards is rapid deployment, given that the filter's response directly influences receiver sensitivity, active component linearity, and spectrum compliance, while compact and trustworthy bandpass solutions are necessary for the current 5G hardware landscape [1]. Due to a trade-off in coverage and capacity, the leading choice to supply commercial networks is FR_1 (Sub-6 GHz) mid-band from 5G. Globally emerging, the n77 (3.3-4.2GHz), n78 (3.3-3.8 GHz), and n79 (4.4-5.0 GHz) bands are effectively chosen regions for enhanced Mobile Broadband (eMBB) and Fixed Wireless Access (FWA). A front-end targeting these spectrums needs to achieve wideband coverage throughout the mid-band or must support multi-band operation to realize the operator's coexistence plans, as the half-spectrum bands differ from region to region. Consequently, 5G FR_1 filters will have to render their maximum transmission, supporting appropriate impedance matching, an insertion loss that is minimally low, steep skirts, considerable blocking, and that in a rather large range of physical dimensions, economically tied design [2].

For FR_1, planar filters are an excellent option due to their reduced height and ease of fabrication using common PCB methods; nonetheless, conventional planar resonator configurations often struggle to effectively suppress spurious signals in broad or multi-band responses. With an increasing number of resonators within the filters in the quest to make them more selective, other filter-contributing mechanisms, such as parasitic coupling, discontinuity effects, and higher-order resonant modes, can come into play to create unwanted transmission windows and equally degrade the stopband. These effects are much more pronounced when working on cheap substrates such as FR-4, as the material exhibits its characteristic dielectric dispersion and loss, making the final insertion-loss performance of a filter inferior by design.

Metamaterial-inspired resonator structures offer an effective way of overcoming such limitations by enabling strong, compact resonances that can be engineered geometrically. SRRs exhibit significant dispersions around the frequency of resonance, primarily because of the inductive loop path and capacitive split-gap. As yet another advantage, especially on coupling into a microstrip line, whereas basic SRRs act as perfect BPFs, bringing frequency-selective features, giving better control over the transmission poles and zeros. Additionally, cascading the SRR unit cell along the direction of propagation provides controlled coupling among resonant elements; hence, such behaviour of multiband and more effective filter order can be achieved without the need for the complex multilayer structure [3].

However, despite these benefits, the control of unwanted spurious responses is still one of the main concerns for real-world applications. Although DGS induces stop-band enhancement more compactly and in a more fabrication-friendly manner by introducing return-current perturbations and thus creating frequency-dependent impedance discontinuities, a judiciously engineered DGS pattern can supress out any of the undesired mode, including a transmission zero, much to clear the upper stopband and maintaining a simple planar layout.

Based on this motivation, the present work proposes an experimentally validated multiband microstrip BPF using a cascaded SRR unit-cell array and a T-shaped DGS for 5G FR_1 n77, n78, and n79 bands. The SRR unit-cell array is used to realize the required multiband resonant behaviour, while the T-shaped DGS is incorporated to suppress unwanted higher-frequency spurious responses and enhance stopband attenuation. The complete filter is designed and optimized using Ansys HFSS, fabricated on an FR-4 substrate, and measured using an Anritsu MS46122B VNA.

The main novelty of this work lies in the combined use of SRR unit-cell-driven multiband passband generation and T-shaped DGS-assisted stopband suppression in a simple planar FR-4 structure. Unlike many existing SRR filters that are designed for single-band operation, lower-frequency wireless bands, narrow fractional bandwidth, or low-loss Rogers substrates, the proposed design targets practical 5G FR_1 mid-band operation using a low-cost substrate and experimental validation. The work also includes SRR unit-cell effective-parameter analysis, electromagnetic field verification, fabrication, measured S-parameter comparison, and benchmarking with reported filter technologies.

2. Existing Approaches and Limitations

2.1. Practical Limitations of Lumped-Element Filter Realizations in Sub-6 GHz 5G Front Ends

A miniature tri-band BPF operates at 0.8 GHz, 1.8 GHz, and 2.6 GHz and was made with surface-mount components on a Rogers 4003C substrate with a thickness of 0.51 mm and a 15 mm × 20 mm area [4]. From three Lowpass Filter (LPF) portions, a BPF is designed. Resonators with shunt topologies provide transmission zeros between passbands to improve isolation and reduce interference. For all three frequency bands, the reflection loss is about 15 dB, whereas the insertion loss is 1.1, 1.4, and 1.2 dB at 0.8, 1.8, and 2.6 GHz, respectively. The system has 290 MHz bandwidth at 0.8 GHz, 1.8 GHz and 1 GHz at 2.6 GHz.

The researchers developed a filter that does not reflect signals [5]. Traditional filters reflect signals, but the suggested structure absorbs them to identify stopband energy. Besides symmetrically placed shunt inductors and series capacitors, LPFs can have reactive elements added for tuning flexibility. By cascading filter sections for specified lower and upper pole frequencies, the BPF is achieved.

Design uses even-odd mode analysis, which necessitates testing both ports with two approaches. Superimposing the even- and odd-mode solutions yields the symmetric two-port network's answer. The LPF has a peak stopband rejection of 53 dB, and the BPF 43dB. In their operational passband, the filters have 25 dB return loss. The LPF has a maximum attenuation point at 325 MHz, and the BPF has two cutoff frequencies at 110 and 310 MHz, creating a 200 MHz bandwidth.

Research in [6, 7] is being developed for mm-wave 5G small cell networks. An LPF and two BPFs target the 28 GHz and 39 GHz frequency bands, respectively. All filters are made using the Semi-Additive Process (SAP), which ensures accurate dimensional measurements throughout production runs. To work, the LPF needs 4.23 × 1.42 mm^2, the interdigital BPF 3.06 × 2.26 mm^2, and the hairpin BPF 3.85 × 1.22 mm^2. LPF design works at 29.5 GHz using normalized prototype g-values to extract inductance and capacitance values for guided wavelength microstrip dimension calculation.

The 28 GHz interdigital BPF uses parallel quarter-wavelength short-circuited resonators with adjustable spacing to vary coupling strength and bandwidth. The system creates an abrupt roll-off and continuous in-band ripple with a Chebyshev response. To reduce circuit size, designers constructed U-shaped half-wavelength resonators employing Chebyshev polynomials for the 39 GHz hairpin BPF. Insertion loss values for the LPF, interdigital BPF, and hairpin BPF are

2.0, 2.6, and 1.4 dB, respectively, whereas reflection loss values are 1517 dB. The interdigital BPF has 18% fractional bandwidth, and the hairpin BPF 16%.

BPFs based on lumped elements are not as useful as one might assume when the operational frequency moves over into microwaves and 5G, because real-world components no longer behave as simple L and C elements. Real inductors and capacitors have substantial parasitic inductance and capacitance at high frequencies, decreasing filter performance. As the parasitic impedance at the self-resonant frequency is higher, it results in decreased efficiency, inappropriate passband characteristics, and higher insertion loss. The majority of inductors, capacitors, and resistors in a network are thought to aid in the creation of compact circuits at low frequencies, but at high frequencies, the size and construction of components resemble the wavelength, making design and repeatability difficult. Because lumped networks have at least two practical limitations, lack of practical tunability and high sensitivity to realization deviations, realizing exact wideband bandwidth control for many 5G applications is difficult. The skin effect increases high-frequency insertion loss due to conductor losses in the trace and dielectric losses in the capacitor and inductance cores, reducing filter efficiency. The lumped element solutions' advantage of minimum PCB space and construction complexity for miniature high-frequency RF front ends is negated by the need for numerous inductors and capacitors.

2.2. Challenges of Cavity Resonator Filters for 5G FR1 Miniaturized Hardware

A mode-splitter structure and dual coupling techniques are used in a tunable Ka-band cavity BPF that uses TE_{011} mode resonators [8]. TE_{011} is chosen because it has reduced insertion loss and is less susceptible to degenerate TM modes. To prevent mode degeneracy, the cavity end walls use a metal-ring mode splitter with a peripheral channel and central bore. The technology couples energy between resonators using short and long irises. A sliding contact mechanism provides electrical continuity during frequency tuning, and a moveable tuning plate on plungers alters the effective cavity length. To improve stability and reduce dimensional sensitivity, the system uses extended irises to connect all coupling paths, creating a pseudo lowpass filter. The filter design uses a pseudo-High-Pass Filter (HPF) with a wide iris for sequential coupling and a smaller for cross-coupling. From 20 GHz to 500 MHz, the filter's center frequency can be modified, and its bandwidth can be tuned between 40 and 160 MHz. The system has 0.3 dB insertion loss and 17 dB return loss. The filter, built using typical precision machining methods, measures 110 × 22 × 20 mm³.

A Ka-band cavity filter resolves performance concerns with typical TE_{011} and TE_{1N} dual-mode filters in [9]. The design employs the TE_{221} mode because its unloaded quality factor is 50% higher than the TE_{011}. TE_{221} modes at orthogonal angles are coupled intra-cavity to create dual-mode functionality. Inter-cavity coupling uses end-wall and side-wall irises to connect adjacent hollow walls. A four-pole filter has four resonator cavities connected by radial and angular irises. The filter operates at 19.9 GHz, with 0.4 dB insertion loss, 17 dB return loss, 44 MHz bandwidth, and 140 × 145 × 25 mm³ physical space.

In [10], two new cavity filter designs were created using inline and vertical layouts to improve space savings and system performance. Engineers place end-launched ports in straight lines in the inline configuration, while angular irises improve inter-cavity coupling and prevent undesired signals. The vertical layout uses side-launched ports to place all connections on one side of the structure, reducing space. A 2A1R iris construction improves signal rejection outside its frequency range. The inline filter is 145 × 35 × 25 mm³, whereas the vertical pattern is smaller at 35 × 35 × 25 mm³.

In [11], a stepped circular waveguide dual-mode filter design for Ku-band applications increases the capability of conventional filters. Cavity step designs reduce spurious signals and expand design possibilities. Iris coupling transfers energy across cavities, and tuning screws near the electric field peak points allow designers to maintain equal phase between overlapping modes and set operational frequencies. The filter operates at 10.73 GHz, with 0.5 dB insertion loss, 17 dB return loss, 54 MHz bandwidth, and 208 × 30 × 30 mm³ volume.

A high-Q Hybrid Resonator (HR)-based BPF is used to produce a compact diplexer with great selectivity and decreased dimensions [12]. A hybrid resonator uses microstrip line and short-circuited coaxial line technology to create a high-Q element that improves system quality. Mixed electromagnetic coupling creates fine selectivity and a wider bandwidth by combining electric and magnetic coupling. RT/Duroid 5880 substrates with 0.508 mm thickness and 2.2 relative permittivity are used to make the filters, which are enclosed in metal to prevent external influence. The diplexer, with a 27.1 × 1.8 × 10 mm³ volume, achieves 1.5 dB insertion loss and 40 dB channel isolation, with passbands of 80 MHz and 102 MHz at 2.4 GHz and 2.7 GHz center frequencies.

[13] improves the hybrid resonator system from [12] by adding shape deformation algorithms to improve filter performance. Because the deformation approach uses control points and displacement vectors to change three-dimensional shapes, the resonator structure and coupling mechanisms remain the same. This approach lets resonators and waveguides bend, twist, and compress while better separating fundamental and higher-order modes. Through cavity geometry optimization, optimal cavity designs produce wider spurious-free regions and better-quality factors. The filter operates at 14.25 GHz with 0.5 dB insertion loss, 17 dB return loss, 54 MHz bandwidth, and 18.77 × 18.77 × 12.72 mm³ dimensions.

The primary issue with cavity resonator-based filters is that they are constrained to small, integrated RF front-end designs for low insertion loss and high selectivity. It follows that they are molded as very big electrical cavities in metal, which are huge and unsuitable for anything that requires synergy across footprints and size with precise integration in a limited space. As they are utilized, properties increase orbital width, leading to working frequencies exceeding 6 GHz, where further smaller cavities are needed. Due to frequency scaling, hardware weight and volume increase, making it economically unappealing for packaging. High-precision requirements for consistent quality performance are most important in that industry. CNC milled, tight-tolerance machining, and post-fabrication tuning using screws or tuning elements increase complexity, time, and cost with multiple serial tunings at production time. PCB-based 5G RF modules are challenging to integrate with because small microstrip/stripline layouts and system-on-package techniques are better for miniaturization and mass production. They are less feasible as a candidate in 5G applications for front-end design scale, short height, and production-friendly prospects due to their narrow band behavior, larger dimensions, and higher manufacturing costs.

2.3. Bandwidth and Loss Challenges of SAW and BAW Filters for 5G n77/n78/n79

The filter design starts with a lowpass Bessel prototype, an all-pole structure tuned for a flat group delay response [14]. The technology converts lowpass response to a BPF using frequency transformation. Instead of LC resonators, the Bessel-type BPF uses SAW or BAW resonators. The practical implementation employs a Cu-grating on a 15°YX-cut $LiNbO_3$ substrate, chosen for its strong electromechanical coupling in SH SAW modes. From the 980 MHz midpoint, group-delay changes of 3 nanoseconds were observed over 15 megahertz. The filter has a 4 × 2 mm² size, 5.3 dB insertion loss, 15 dB return loss, and 30 MHz bandwidth.

A hybrid RF filter design method using high-Q SAW resonators and lumped-element impedance inverters is described in[15]. The technology eliminates the biggest drawbacks of ladder and lattice acoustic filters: restricted fractional bandwidth and group-delay fluctuations. The design heavily uses Acoustic Wave Lumped Resonators (AWLRs) connected by impedance inverters with discrete inductors and capacitors. Impedance inverters are crucial for bandwidth management and group-delay response flattening. Two AWLRs connected through three impedance inverters form the two-pole bandpass filter, which was built on a Rogers RO4003 substrate with a thickness of 1.52 mm and a dielectric constant of 3.55. This small 15 × 7 mm² filter runs at 418 MHz center frequency, with insertion loss of 1.5 dB, return loss of 17 dB, and 450 MHz bandwidth.

BPF design for 5G applications combining SAW and BAW resonators based on Aluminum Nitride (AlN) is examined in [16]. The study compares Thin-Film Bulk Acoustic Resonators (TFBARs) to Solidly Mounted Resonators. TFBARs employ an air cavity beneath the resonator to confine acoustic energy, while SMRs use Bragg reflectors with many layers of varying impedances to keep it from reaching the substrate. SMRs are ideal for 5G applications due to their mechanical strength and severe temperature performance. The study compares ladder-type, lattice-type, stacked crystal, and coupled-resonator acoustic filters. Ladder-type filters use series and shunt resonators at distinct frequency points to provide a sharp roll-off near the passband but weak signal rejection beyond it. Lattice filters use resonators to improve stopband performance but diminish passband signal selection. Stacked crystal filters use multilayer piezoelectric and metallic sheets for compactness and low insertion loss. Coupled-resonator filters reduce resonator effects and double the bandwidth of stacked crystal filters by coupling through a dedicated layer. Acoustic filters with typical performance tests exhibit insertion loss of 3 dB, return loss of 18 dB, and bandwidth of 5% to 10% of center frequency in a compact 3 × 5 mm² area.

In [17], SAW filter technologies are detailed, focusing on novel material developments, improved manufacturing procedures, and design methodologies to fulfill the operating needs of 5G networks and high-frequency RF systems. Interdigital Transducers (IDTs) and reflectors make conventional SAW filters efficient in low-frequency situations with narrowband signal processing. Multiple resonators and clamping capacitors give dual-mode SAW filters multimode capacity for sophisticated filtering. The industry generally uses $LiNbO_3$ and $LiTaO_3$ substrates for their good piezoelectric coupling, whereas aluminum and Ti/Cu multilayer electrodes are used for their reduced resistive losses.

BAW resonator designs with improved SiO_2/Ta_2O_5 Bragg reflectors are examined in [18] for 5G technology development. SMR-based systems outperform FBARs for frequencies above 3 GHz due to their better structural strength, electromechanical coupling, and multi-frequency operation. The resonator construction uses a Lithium Niobate (LN) thin film between aluminum electrodes, while the Bragg reflector stack switches between low-impedance SiO_2 and high-impedance Ta_2O_5 layers. Using a 5 × 5 mm² area, the 3.5 GHz ladder-type BPF achieved 1.9 dB insertion loss, 19 dB return loss, and 245 MHz bandwidth.

In [19], AlScN-based BAW resonators at 5G frequencies near 3.5 GHz are demonstrated, introducing new developments. Resonators with 28% scandium doping have greater electromechanical coupling than AlN materials. Cross-Sectional Bulk Acoustic Wave (XBAW) resonators reduce energy loss and improve acoustic confinement. The filter delivers 1.2 dB insertion loss, 18 dB return loss, 216 MHz bandwidth, and approximately 15% electromechanical coupling coefficient in a compact 0.8 × 0.8 mm² design. A 5G-specific wideband acoustic transversal filter is shown in [20]. The transversal architecture connects numerous acoustic resonators via parallel branches, creating independent signal channels. Because transmission zero points and bandwidth parameters are not impacted by electroacoustic coupling coefficients, the system allows filter construction with varied filter responses. The technique lets designers develop wideband systems with fewer resonators than before. Resonator frequency optimization, coupling strength, and impedance level changes give the filter 2 dB insertion loss at 3.75 GHz center frequency, 16 dB return loss, and 910 MHz wide passband. A 13% electroacoustic coupling coefficient is observed, using a filter dimension of 0.5 × 0.5 mm².

SAW and BAW filters can overcome several constraints without meeting 5G FR1 mid-band specifications. Most SAW/BAW filters were used in 2G–4G systems. Larger bandwidths are needed for 5G BPFs in the 3.3-4.2-GHz and 4.4-5.0-GHz bands with n77 and n79. Traditional platforms like $LiTaO_3$-based SAW or AlN-thin-film-based BAW struggle to produce wideband filters without significant losses and poor rejection figures. By this, SAW filters can be utilized for a wide range of frequencies, but they have drawbacks over 2 GHz. BAW devices have a higher frequency periodicity than SAW devices, but expanding them for full broadband sub-6 GHz 5G operation increases insertion loss and reduces efficiency, which is a concern for successful implementation.

2.4. Suitability of Plasmonic / Waveguide-Inspired Filters for 5G Mid-Band Operation

Microwave BPFs using Substrate-Integrated Plasmonic Waveguides (SIPWs) between 7.5 GHz and 13.0 GHz are studied in [21]. The suggested filter uses copper metallization on a 0.5-mm Rogers 5880 substrate with a relative permittivity of 2.2. Etching regular patterns onto the upper and bottom metal layers of a Substrate Integrated Waveguide (SIW) system creates the SIPW structure and Spoof Surface Plasmon Polariton (SSPP) phenomena. The topology is microstrip–SIW–SIPW–SIW–microstrip. A tapered microstrip-to-SIW transition allows the system to seamlessly switch between quasi-TEM and quasi-TE operational modes for broadband capabilities. A graded slot-length profile allows momentum adaptation and impedance matching from the quasi-TE mode to the SSPP mode during the SIW-SIPW transition. The filter has a center frequency of 10.25 GHz, insertion loss of 1.5 dB, return loss of 10 dB, and over 40% fractional bandwidth in a 36 × 18 mm² footprint.

SIPW and SSPP were utilized to produce a compact but efficient X-band bandpass filter for 7.3 to 10.1 GHz in [22]. Fishbone- and hourglass-shaped grooves improve electromagnetic field management and signal coupling, allowing mushrooming-faced slot antennas to broadcast military messages. The filter is made of 0.5-millimeter FR-4 with a dielectric constant of 4.3. A fishbone-shaped transition area connects microstrip lines to SSPP/SIPW transmission paths, a filtering area with hourglass-shaped grooves enables SSPP-based bandpass operations, and the system's main transmission path is the SIPW section. The filter center frequency is 8.7 GHz. It has about 2 dB insertion loss. The return loss is about 10 dB. The system offers 32% fractional bandwidth. The device occupies a 34.4 × 12.2 mm² area.

The microwave BPF design in [23] uses SSPP transmission lines with Rogers 5880 substrate material with 1.5 mm thickness and 2.2 dielectric constant. A unique H-shaped SSPP unit cell is used in the filter, which operates at microwave frequencies between 1.2 GHz and 6.0 GHz. The system has four components: a Coplanar Waveguide (CPW) feed for 50-Ω impedance matching, a transition section for mode conversion between CPW and SSPP, a periodic SSPP transmission line for plasmonic wave movement, and an LC resonator for bandpass filtering. The filter has a 2 dB insertion loss, 10 dB return loss, and 41% fractional bandwidth in a 26 × 4 mm² size. Researchers use Planar I-Shaped Plasmonic Waveguides (PIPWs) to create ultra-strong electromagnetic field confinement with low propagation loss [24]. The I-shaped groove has lateral extensions at both ends to increase capacitive loading and electric field spatial control. The filter structure has a CPW feeding portion, a transition zone for quasi-TEM to SSPP mode conversion, and an SSPP transmission-line section. The filter operates from 1 to 5.2 GHz on an F4B substrate with a relative permittivity of 2.65 and a thickness of 0.5 mm. The insertion loss is around 1.5 dB, the return loss is around 12 dB, and the fractional bandwidth is at 42%, despite the larger size of 104 × 35 mm².

Despite their field confinement benefits, plasmonic filters cannot fully utilize their claim for sub-6 GHz applications for 5G systems' front modules due to their structure. Plasmonic waveguides may have higher propagation loss due to higher effective resistance, ohmic dissipation, and mostly restricted efficiency confinement of plasmonic mechanisms at longer wavelengths, which increases signal attenuation, which is undesirable in 5G receivers and transmitters, where low-loss filtering is essential. Further plasmonic filters are challenging to build on 5G RF platforms due to their complicated metallic groove patterns, subwavelength structuring, and PCB fabrication procedures. Complex geometries require complex and costly fabrication because specific patterning of features like hourglass, fishbone, or groove-based structures increases process sensitivity and reduces manufacturing tolerances. In a scalable and commercially viable 5G system implementation at sub-6 GHz, plasmonic filters are less desirable because of their higher loss, PCB integration complexity, and higher production cost.

2.5. Performance Bottlenecks in Conventional Planar Resonator Filters

The creation of a parallel-coupled dual-mode resonator BPF is examined in [25]. Dual-mode resonators provide two non-degenerate resonant modes, allowing higher-order filtering responses with fewer physical resonators. The dual-mode resonator circuit has two coupled resonators connected by an admittance inverter and susceptance elements. The design creates a four-pole microstrip bandpass filter on a RO4003C substrate with a relative permittivity of 3.36 and a thickness of 0.5 mm to obtain a 1 GHz center frequency. Due to fabrication tolerances, dielectric constant change, and coupling imperfections, the center frequency has dropped from 1.0 GHz to 0.968 GHz, according to experimental observations. The filter exhibits significant stopband rejection, with initial spurious answers at $2.88f_0$ and $3.12f_0$ instead of $2f_0$, indicating improved harmonic suppression. Measured insertion loss is 2.5 dB, return loss is 15 dB, bandwidth is 98.6 MHz, and physical size is 30 × 20 mm².

Ultra-Wideband BPFs (UWB) use tapered transmission-line resonators to operate from 3.1 GHz to 10.6 GHz, according to [26]. Compact tapered resonators offer greater stopband performance and a wider operational range than typical transmission-line resonators. Exponential Tapered Transmission Lines (ETTLs) vary impedance through their resonator length, while Linear Tapered Transmission Lines (LTTLs) change impedance linearly. UWB BPF uses tapered resonators instead of standard elements with different taper ratios to change bandwidth and stopband performance. Higher taper ratios extend bandwidth and reduce out-of-band interference. Four short-circuited tapered stubs connect through uniform transmission-line sections less than half their length to produce the filter structure. Rogers RT5880 substrates with 2.2 relative permittivity and 0.78 mm thickness were used to build the filter. The filter operates at 6.8 GHz with a 2.5 dB insertion loss and 15 dB return loss, fitting within a 30 × 20 mm² space.

In [27], the system introduces a multilayer ultra-broadband bandpass filter which uses high impedance slot-line resonators to achieve two aims, which are lowering radiation loss and enhancing stopband performance. The revised resonator design replaces the single short-circuited high-impedance slot-line segment with two shunt-connected folded low-impedance slot-line sections to reduce radiation and improve microstrip circuit impedance matching. The research team constructed an ultra-wideband microstrip-to-microstrip vertical transition to connect slot-line resonators to multilayer filter systems. The transition design uses coupled microstrip and slot-line resonators as its base model, which provides complete broadband functionality. The seven-pole Chebyshev equiripple BPF uses a Rogers 4003C substrate with 2.2 relative permittivity and 0.81 mm thickness. The filter has a 21 × 10 mm² size and operates at 2 GHz with 1.3 dB insertion loss and 13 dB return loss.

The microstrip bandpass filter in [28] uses a polygonal open-loop resonator to improve size efficiency and passband operation for Bluetooth and WLAN. The suggested filter uses two polygonal open-loop resonators with 11 different-length segments to vary electrical length without adding space. This approach lets open-loop resonators operate at smaller sizes with selective performance and low insertion loss. At 2.4 GHz, the filter operates on a Rogers RO3010 substrate with a dielectric constant of 10.2 and a thickness of 1.5 mm. The results show that the system achieves a bandwidth of roughly 230 MHz with an insertion loss of 1.2 dB and a return loss that exceeds 25 dB while the system occupies a small space of 8 × 16 mm².

Parallel-coupled line filters and dual-mode resonators have numerous drawbacks when applied to sub-6 GHz 5G front-end requirements. Many planar resonator topologies are naturally suited to narrowband operation, and extending them to 5G bandwidths often requires stronger coupling and additional resonator sections, which can increase design sensitivity and loss. Insertion loss becomes a major concern above 3 GHz because conductor losses (skin effect, surface roughness) and dielectric losses accumulate along distributed resonator paths. 5G systems require a low-loss RF chain for receiver sensitivity and transmitter efficiency. Planar resonators support higher-order modes that can create unwanted transmission windows outside the desired passband, causing harmonic and spurious response production. Extra resonators, defective ground structures, or filtering sections are needed to suppress these spurious harmonics, which increases circuit complexity, footprint, and optimization and fabrication for practical RF modules.

2.6. Electromagnetic Resonator–Based Filters using SRR / CSRR for 5G Mid-Band Front Ends

The design of a 2.4 GHz SRR BPF is provided in [29]. Ring length, width, gap, and inter-ring spacing determine the resonant behavior of the SRR unit's two concentric rings, an outer and an inner. The filter's coupling strip controls energy transfer between the SRR and the feeding structure. To connect to external circuits, the filter uses a microstrip transmission line. The sequential arrangement of three SRR components with optimal inter-element spacing increases filtering performance. The filter utilizes a 25 × 19 mm² Rogers RT/Duroid 6010/6010LM substrate with a 10.2 relative permittivity and 1.9 mm thickness. The measured findings show 2.5 dB insertion loss, 16 dB return loss, and roughly 5% fractional bandwidth.

A parallel-coupled microstrip BPF with SRR and Complementary Split Ring Resonator (CSRR) elements has been used to create a 1 GHz operating system [30]. Parallel-coupled microstrip lines form the system's passband. Engineers put two stepped-impedance stubs symmetrically to improve selectivity around the resonator point. The basic system design generates undesirable harmonics and fails to reject signals outside its stopband range, however SRRs, CSRRs, and stepped-impedance stubs fix these problems and improve performance. The system uses SRR and CSRR elements to provide low insertion loss and excellent stopband rejection between 1.22 GHz and 5 GHz. The filter uses FR-4 substrate material with a dielectric constant of 4.4, thickness of 1.6 mm, and a space of 30 × 18 mm². It has an insertion loss of 1.1 dB, a return loss of around 16 dB, and a fractional bandwidth of 21%.

The article describes a narrowband X-band BPF with two circular SRR rings in [31]. A microstrip feedline excites and matches the resonator's impedance. The filter response is adjusted by systematic change of SRR parameters such as ring gap, width, and spacing. Increasing the ring gap or breadth raises the resonant frequency, while lowering them lowers it. After changing the inter-ring spacing, the central frequency remains unchanged. The filter is constructed on Rogers RT/Duroid 5880 substrate, with a 2.2 relative permittivity, 0.5 mm thickness, and 25 × 22 mm² area. The observed center frequency is 9.0 GHz, with an insertion loss of 3.7 dB, a return loss of 15 dB, and a narrow fractional bandwidth of roughly 1%.

A dual-band BPF is created by electromagnetic coupling between twin SRRs and CSRRs in [32]. The first arrangement uses twin SRRs with weak coupling because their outward-facing gaps provide two passbands at 5.02 GHz and 8.92 GHz. When oriented to face each other, SRR gaps couple better, expanding the lower band range from 230 MHz to 320 MHz. Because it generates a notch-filtering effect that eliminates undesirable signals throughout the passband, a CSRR improves twin SRR coupling. The filter creates more exact transitions and improves signal separation. The 16 x 24 mm² filter, built on Rogers RO4003 substrate with 3.55 dielectric constant and 0.85 mm thickness, exhibits 6.22 dB and 5.23 dB insertion losses in lower and upper bands, respectively, with 6% and 3% fractional bandwidths.

[33] shows a circular SRR-based microstrip BPF. The major resonating element is the SRR, which has two concentric rings with capacitive gaps. Microstrip feedlines with 50 Ω impedance power the resonator. The capacitive gaps and inductive rings form an LC resonant circuit that sets the operation frequency. Rogers RT/Duroid 6010 substrate, with 11.4 relative permittivity and 1.9 mm thickness, is used to build a 25 × 25 mm² filter design. The experimental results show a 2.4 GHz center frequency, 1.3 dB insertion loss, 18.8 dB return loss, and 5% fractional bandwidth.

Study in [34] explores how substrate permittivity and thickness affect square-shaped double split-ring resonators' performance. When substrate permittivity increases, resonator effective capacitance increases, decreasing resonant frequency and bandwidth. The bandwidth widens, and resonance rises as permittivity decreases. Small effective capacitance increases with substrate thickness decrease, resonance frequency, but improves electromagnetic coupling and fringing fields to increase bandwidth. Thinner substrates have better confinement and fewer losses but lower coupling strength. Parallel-coupled lines with two CSRRs carved into the ground plane form a BPF system [35]. The microstrip-linked lines allow signal flow and interaction, while the CSRRs add resonant routes for selectivity and bandwidth management. Parametric optimization of CSRR size and coupling gaps improves impedance matching and reduces insertion loss. The filter, which uses a 0.5-mm Rogers RT/Duroid 5880 substrate, operates at 3.6 GHz with an insertion loss of 1.6 dB, a return loss of 17 dB, and a fractional bandwidth of 5% in a 27 mm × 14 mm region.

The effect of adding SRRs to a microstrip structure is studied in [36] using an SRR-based band-stop filter. Attenuation and stopband are limited by a single SRR, although electromagnetic coupling and resonance strength increase with more SRRs. Three SRRs produce 19 dB attenuation, whereas six SRRs produce 30 dB rejection with an expanded stopband. Advanced connections between numerous SRRs increase energy absorption and stopband performance.

[37] offer a multiband SRR BPF design for 2.4 GHz, 4.5 GHz, and 5.2 GHz. Three SRR unit cells with distinct resonance frequencies are used. An etched slot near the center of the microstrip transmission line improves frequency selectivity in the system's primary signal channel. The analysis demonstrates that SRR width improves return loss and length improves insertion loss. The filter, built on a 1.6 mm FR-4 substrate, occupies a 26 × 18 mm² space and exhibits insertion losses of 1.0 dB, 1.4 dB, and 2.1 dB across its three operational frequency bands.

Metamaterials and SRR arrays connected to a microstrip line are used to create a cut-band filter in [38]. The study explores how SRR numbers, dimensions, and positioning patterns affect bandwidth and rejection. Through better coupling, additional SRRs improve rejection performance, while varied sizes prolong the stopband. Multiple SRR rows improve electromagnetic interaction and rejection performance without adding filter design space. The balance between high rejection depth and passband performance is shown by excessive SRR stacking, which lowers transmission levels.

The latest SRR/CSRR compact microwave filter improvements still have major limitations. This limits direct use for mass and efficient deployment in sub-6 GHz 5G front-end modules. Most SRR-based filters are for low-frequency wireless bands or have tiny fractional bandwidths. This limits 5G FR1 and n77/n78/n79, which need higher bandwidths and stable in-band transmission. Most current implementations use a single or loosely coupled SRR-based resonator setup, which results in low electromagnetic coupling strength, slow roll-off, and poor transmission zero control needed for tight adjoint-channel and complete out-of-band suppression.

Advanced cascaded SRR tends to give a filter high handle selectivity and out-of-band rejection, but insertion loss, fabrication tolerances, and footprint will increase, which compact 5G RF modules must avoid. The relationship between SRR/CSRR loading and practical microstrip feeding networks is rarely studied, giving a leverage disadvantage under optimal impedance match and tuning control for all 5G bands. These limits emphasize the need for sophisticated 5G architectures with strongly and densely coupled resonators on a planar path. Bandpass filter topology of practical microstrip feed and ground structures promises wideband/multiband operation, low insertion losses, considerable selectivity, and excellent out-of-band suppressions in a small and fabrication-friendly form.

2.7. Gap Analysis Leading to the Proposed Multiband BPF

The currently available filter solutions for the 5G FR_1 mid-band still display a mismatch among band coverage, stopband cleanliness, size/cost or practical validation.

Lumped-element filters are unsuitable in 5G frequencies since the parasitics and self-resonance degrade the matching and insertion loss of the filter, making wideband or multiband behavior very difficult.

Cavity-resonator filters provide the best selectivity. Yet, these filters have a big size, are costly to manufacture or tune, which in turn creates integration problems with the planar 5G RF modules, which conflict with compact front-end requirements.

SAW/BAW technologies are not good at providing the wide bandwidth necessary for the n77/n78/n79 bands in sub-6 GHz without severe loss and performance trade-offs or difficulties in scaling beyond ~3 GHz.

Although plasmonic/SIPW/SSPP-inspired filters can be attractive choices for confinement, the complex patterning and integration challenges are often a drawback, making them not so attractive to low-cost 5G PCB-level implementation.

Meanwhile, conventional planar resonator filters are generally single-band and susceptible to undesirable higher-order modes; suppressing these requires additional structures with increased footprint and design complexity.

In metamaterial-inspired solutions, several reports show SRR/CSRR filters with low bands and fractional bandwidths and are based on single coupled resonators or very weakly-coupled ones, producing less steep skirts and reduced control of transmission zeros, which are mandated for out-of-band strict suppression. Furthermore, multiple SRR cascaded can further enhance rejection, but with higher insertion loss, increased sensitivity to different fabrication tolerances, and a need for much larger layouts.

The multiband filter proposed in this work is aimed at the development of a compact, planar, and experimental solution that can show its feasibility for mid-band operation in 5G FR1 bands n77, n78, and n79 without the limited design choices of lumped elements through the bulk and cost powers of cavity-like structures.

The novelty of the proposed work is to convert the SRR unit cell resonance to a controllable multiband reaction through the cascaded SRR array and to enhance stopband suppressions through a T-shaped DGS. This addresses head-on the shortcomings being encountered in the literature: poor bandwidth or coverage; weak control of transmission zeros; and improper spurious suppression while keeping the structure compatible with common PCB technology for practical 5G front-end implementation.

3. Design Analysis of the Split-Ring Resonator Unit Cell

The SRR functions as a crucial element in metamaterials that facilitates the development of Left-Handed Materials (LHM). SRRs comprise two metallic rings that manifest as concentric circles or square configurations. The ring construction features a gap that generates the capacitance. Figure 1 depicts the square-shaped SRR [39].

The electric field distribution is uniform due to the symmetrical arrangement of gaps ‘g’. The structure employs opposing gaps to stabilize the system by inhibiting energy dissipation. The two rings preserve their orientation due to the generation of substantial magnetic flux via induced currents, which reinforces the overall magnetic field of the system.

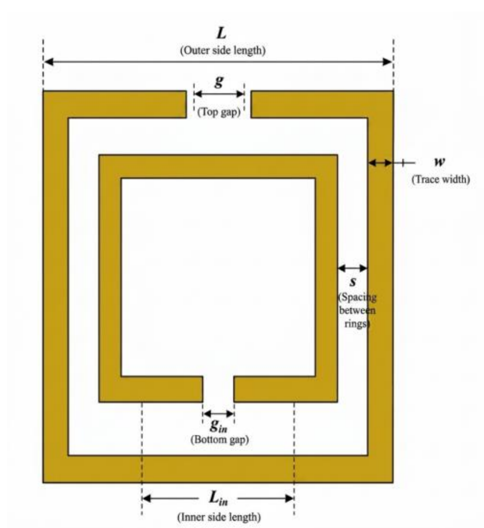

Fig. 1 Geometry of Square-Shaped SRR

The reduced inter-ring spacing ‘s’ facilitates enhanced electric field regulation, enabling SRRs to operate as efficient metamaterial waveguides by concentrating localized fields.

The spacing between rings influences the strength of their magnetic coupling. The rings exhibit enhanced mutual inductance due to a reduction in their ‘g’ value, resulting in intensified resonance effects with more profound resonance patterns. The electric field is more firmly constrained inside a limited ring width 'w', resulting in an electric field distribution pattern that aims to reduce spatial dispersion. A broader ring diminishes its inductance per unit length, resulting in diminished magnetic field control, whereas a narrower ring enhances its capacity to link magnetic flux.

The inductive (L) and capacitive (C) characteristics essentially tune the SRR's resonance frequency, f_0. The relationship is provided as [39].

$$f_0 = \frac{1}{2\pi\sqrt{LC}} \tag{1}$$

where the parameters of the ring gap ‘g’ and inter-ring spacing ‘s’ form C, and the dimensions of the ring width ‘w’ and length ‘L’ determine L.

The separation 'g' establishes a capacitance C_{gap} defined by [39].

$$C_{\text{gap}} = \frac{\varepsilon_0 \varepsilon_r A}{g} \tag{2}$$

where ‘A’ represents the capacitor’s cross-sectional area, and ε_r indicates the dielectric material’s relative permittivity.

Wider gaps decrease capacitance, raising the resonance frequency f_0. However, a shorter gap increases capacitance and lowers resonance frequency f_0.

To control the inner-outer rings mutual capacitance C_m, the spacing ‘s’ is utilized [39].

$$C_m = \frac{\varepsilon_0 \varepsilon_r (2(\text{L} + L_{\text{in}}) - s)}{2s} \tag{3}$$

As the mutual capacitance increases due to reduced separation, the resonance frequency f_0 decreases. On the flip side, when the distance between the elements is larger, the mutual capacitance is lower, leading to a higher resonance frequency f_0.

The structure's inductance L_m is affected by the ring width ‘w’ [39].

$$L_m = \mu_0 (\text{L} + L_{\text{in}}) \frac{w}{s} \tag{4}$$

Because wider rings have lower inductance, they raise the resonance frequency f_0, while narrower rings decrease it.

Total inductance depends on ring length [39].

$$L_m \propto \text{L} + L_{\text{in}} \tag{5}$$

Longer rings increase inductance, decreasing resonance frequency f_0. In contrast, shorter rings decrease inductance and increase resonance frequency f_0.

Hence,

$$f_0 = \frac{1}{2\pi\sqrt{L_{\text{eq}} C_{\text{eq}}}} \tag{6}$$

where $L_{\text{eq}} = \mu_0 (L + L_{\text{in}}) \frac{w}{s}$ and $C_{\text{eq}} = C_{\text{gap}} + C_m$

The NRW [40] method estimates a material's complex permittivity $\varepsilon = \varepsilon_r \varepsilon_0 = (\varepsilon_r' - j\varepsilon_r'')\varepsilon_0$ and permeability $\mu = \mu_r \mu_0 = (\mu_r' - j\mu_r'')\mu_0$ using S-parameters from reflection and transmission measurements.

$$S_{11} = \frac{(1 - P^2)\Gamma}{1 - P^2 \Gamma^2} \tag{7}$$

$$S_{21} = \frac{(1 - \Gamma^2)P}{1 - P^2 \Gamma^2} \tag{8}$$

where $P = e^{-jk_2 d}$ is the propagation factor within the material.

Γ is the interfacial reflection coefficient expressed as:

$$\Gamma = \frac{Z - Z_0}{Z + Z_0} \tag{9}$$

Z represents the wave impedance of the material, while Z_0 denotes the wave impedance of free space.

Establishing the intermediate quantities.

$$V_1 = S_{21} + S_{11} \tag{10}$$

$$V_2 = S_{21} - S_{11} \tag{11}$$

Solving for Γ

$$\Gamma = X + s_1 \sqrt{X^2 - 1} \tag{12}$$

where

$$X = \frac{1 - V_1 V_2}{V_1 - V_2} = \frac{1 - S_{21}^2 + S_{11}^2}{2S_{11}}$$

Solving for P

$$P = \frac{V_1 - \Gamma}{1 - V_1 \Gamma} \tag{13}$$

Evaluating the propagation constant within the material, k_z.

$$k_z = \frac{n-\phi}{2\pi}\frac{1}{d/\lambda_0} + j\frac{\ln|P|}{2\pi}\frac{1}{d/\lambda_0} \quad (14)$$

'd' represents the thickness of the sample, 'λ_0' denotes the free-space wavelength, and 'n' signifies the branch number.

$$\varepsilon_r = k_z F \quad (15)$$

$$\mu_r = \frac{k_z}{F} \quad (16)$$

where 'k_z' is the wavenumber within the material and 'F' is defined as:

$$F = \frac{1-\Gamma}{1+\Gamma} \quad (17)$$

The dimensions of the proposed SRR unit cell are specified in Table 1 and depicted in Figure 4. The resonator employs FR-4 substrate with a thickness of 1.6 mm and a relative permittivity of 4.4 for a center frequency of 4.7 GHz.

Table 1. Dimensions of the SRR unit cell

Parameter	Dimensions
Length of Ring	4.0 mm
Inter-ring Spacing	1.0 mm
Width of Ring	0.7 mm
Gap in Ring	0.5 mm

In order to validate the metamaterial behavior, the effective permittivity and permeability of an SRR unit cell were extracted as observed in Figures 2 and 3. At the center frequency of 4.70 GHz, the extracted effective permeability is ≈ −0.222, which proves the intended magnetic resonance associated with the circulating current in the SRR loop. The imaginary part of effective permeability is ≈ 0.405 near resonance, wherein the energy storage is quite strong. The values of effective permittivity extracted at 4.70 GHz are positive and therefore, with respect to the above, the dominant metamaterial signature at the frequency of operation is of the primarily magnetic type. Furthermore, a higher-frequency resonant feature is observed near ≈ 9 GHz in effective permeability, which provides more proof of a higher-order unit-cell mode that would contribute to the upper-band response of such filters and further add to the stopband behavior.

4. Filter Topology and Working Principle

4.1. Filter Topology

The symmetrical-line microstrip arrangement was used to achieve the BPF design that is depicted in Figure 4. This design was initially modeled and created using Ansys HFSS, and it was then realized on a single dielectric substrate.

In order to excite a cascaded unit-cell SRR array, a microstrip feedline of 50 Ω is positioned in the high-current location, which corresponds to the area where the directed electromagnetic fields are maximized. For the purpose of maximizing the frequency-selective response, multiple SRRs are cascaded in the direction of propagation. This ensures that the traveling wave encounters subsequent resonant cells at various cell resonances. The dimensions of the BPF are indicated in Table 2.

A DGS in the shape of a T is etched beneath and around the transmission line. A longitudinal slot that is aligned across the feedline and a transverse limb form a T-profile. It perturbs the return current distribution along the ground plane. In this case, the SRR array firmly generates the resonance poles resulting from the formation of the multiband passbands, while the DGS provides a means for introducing zeros of attenuation to stifle spurious modes of higher orders and enhance the stopband rejection.

4.2. Resonance Mechanism and Multiband Passband Formation

The working of the BPF is governed by the resonance of SRRs and the ground-plane defect. Each SRR performs as a compact resonator that stores magnetic energy through its loop inductance and electric energy through capacitance. Concentrated capacitance is present across the split gap and inter-ring coupling region of the SRRs. When the SRRs are excited by the microstrip line, magnetic coupling induces current within the SRR loops.

At the resonance, the energy exchange results in a very sharp spectral feature affecting transmission and reflection, characteristic. Cascading SRRs effectively increases the filter order, enabling multiple resonances, improved skirt selectivity, and increased ability to control the passband formation through inter-cell spacing and coupling strength. This is reflected in the evolution of $|S_{21}|$and $|S_{11}|$across frequency.

The T-shaped DGS, operating as a defect in the ground path, introduces a frequency-selective impedance discontinuity, introducing deep transmission zeros that will in turn cancel the parasitic responses. The DGS introduced is mainly dedicated to cleaning the upper stopband, suppressing spurious elements arising from parasitic interactions among SRR cells and microstrip discontinuities, hence enhancing the out-of-band rejection without additional top-layer resonators.

4.3. Suitability for 5G FR1 Bands (n77/n78/n79) and Stopband Control

The mixed SRR-DGS is an optimal topology for 5G FR_1 applications because it has inherent resonance placements for the targeted mid-band allocations. By carefully aligning the SRR and coupling dimensions with the lower and mid bands already within the n77 and n78 regions, an additional tuning of resonant enhancement can take place around 4.4-5.0 GHz, supporting n79. In parallel, a DGS provides solid filtering support through transmission-zero formation, while obfuscating spurious signals far beyond the service bands, making multiband filtering and an application truly versatile for the 5G RF front end operating at sub-6 GHz.

5. Mathematical Analysis

5.1. Microstrip Line Model

Each uniform microstrip section is modeled as a transmission line with ε_{eff}, Z_0, and β. The effective permittivity is approximated by:

$$\varepsilon_{\text{eff}} \approx \frac{\varepsilon_r+1}{2} + \frac{\varepsilon_r-1}{2}\left(1+\frac{12h}{w}\right)^{-1/2} \tag{18}$$

The guided wavelength and phase constant are:

$$\lambda_g = \frac{c}{f\sqrt{\varepsilon_{\text{eff}}}}, \beta = \frac{2\pi}{\lambda_g} \tag{19}$$

A transmission-line section of electrical length $\theta = \beta\ell$ has an ABCD matrix.

$$\mathrm{M}_{\mathrm{TL}} = \begin{bmatrix} \cos\theta & jZ_0\sin\theta \\ j\frac{1}{Z_0}\sin\theta & \cos\theta \end{bmatrix} \tag{20}$$

5.2. SRR Unit-Cell Equivalent (LC Resonance)

The SRR can be modeled as a resonant RLC branch,

$$Z_{\text{SRR}}(\omega) = R + j\omega L + \frac{1}{j\omega C} \tag{21}$$

The resonance occurs when the imaginary part is zero.

$$\omega_0 = \frac{1}{\sqrt{LC}}, f_0 = \frac{1}{2\pi\sqrt{LC}} \tag{22}$$

Geometrically, the SRR resonance is governed by its effective inductance L and capacitance C. The inductance primarily increases with the current-loop length, whereas the capacitance increases when the split gap and inter-ring spacing are reduced, because tighter gaps strengthen electric-field concentration and coupling. As a result, the resonant frequency follows. $f_0 = \frac{1}{2\pi\sqrt{LC}}$ when either L and/or C decreases, the product LC reduces and f_0 shifts upward, while an increase in L and/or C enlarges LC and shifts f_0 downward.

5.3. DGS Equivalent (Ground Plane Resonant Defect)

A DGS introduces a resonant perturbation commonly represented by an equivalent parallel LC in the ground-return path. In a simplified form, its frequency-selective behavior may be represented by an admittance.

$$Y_{\text{DGS}}(\omega) = G + j\omega C_{\text{d}} + \frac{1}{j\omega L_{\text{d}}} \tag{23}$$

The DGS resonance is:

$$Y_{\text{DGS}}(\omega) = G + j\omega C_{\text{d}} + \frac{1}{j\omega L_{\text{d}}} \tag{24}$$

At near ω_{d}, The defect strongly disturbs current return, leading to a transmission zero or deep attenuation, thereby strengthening stopband suppression.

5.4. Network Representation Using ABCD

When the SRR and DGS are treated as shunt loading effects, the corresponding shunt element matrix is,

$$\mathrm{M}_{\text{shunt}}(Y) = \begin{bmatrix} 1 & 0 \\ Y & 1 \end{bmatrix} \tag{25}$$

A loaded section can be written as:

$$\mathrm{M}_{\mathrm{TL}}(\theta_1)\mathrm{M}_{\text{shunt}}(Y_{\text{SRR}})\mathrm{M}_{\text{shunt}}(Y_{\text{DGS}})\mathrm{M}_{\mathrm{TL}}(\theta_2) \tag{26}$$

For an array of N SRR unit cells, the overall ABCD matrix is,

$$\mathrm{M}_{\text{tot}} = \prod_{k=1}^{N} \mathrm{M}_{\text{sec},k} = \begin{bmatrix} A & B \\ C & D \end{bmatrix} \tag{27}$$

5.5 Conversion to S-Parameters

With reference impedance Z_0, the scattering parameters are,

$$S_{21} = \frac{2}{A+\frac{B}{Z_0}+CZ_0+D} \tag{28}$$

$$S_{11} = \frac{A+\frac{B}{Z_0}-CZ_0-D}{A+\frac{B}{Z_0}+CZ_0+D} \tag{29}$$

Equations (27)-(28) show that passbands occur when the denominator magnitude is minimized (constructive transmission), while deep stopbands occur when the denominator becomes large, often due to large shunt admittances introduced near SRR/DGS resonances.

5.6. Interpretation of Multiband Behavior and Stopband Suppression

Multiband passband formation in the proposed filter is primarily attributed to the presence of multiple SRR resonances along the microstrip line. Each SRR cell introduces a distinct resonant mode, and when several cells are cascaded, their mutual coupling can split and redistribute these modes across the frequency axis, effectively generating multiple transmission poles within the targeted spectrum. This cascaded arrangement also increases the effective filter order, which sharpens the transition skirts and improves selectivity compared with a single-resonator implementation. In addition, the stopband performance is strengthened by the DGS, whose resonance perturbs the ground-return current and introduces transmission zeros. These zeros suppress unwanted spurious transmission paths and higher-order parasitic modes, thereby increasing attenuation outside the desired passbands and yielding enhanced out-of-band rejection.

5.7. Practical Loss Model for Measurement Correlation

Measurement differences are explained by finite losses and parasitic. A compact resonator quality factor description is:

$$Q \approx \frac{\omega_0 L}{R} \approx \frac{1}{\omega_0 RC} \quad (30)$$

Additionally, the propagation constant becomes $\gamma = \alpha + j\beta$, broadening resonances and increasing insertion loss relative to ideal simulations.

6. Results and Discussion

6.1. HFSS Simulation and Optimization Workflow

Ansys HFSS is used to simulate the proposed SRR-DGS BPF using a 2-port excitation. The design was further optimized in two consecutive steps. The objective of the first step is to establish a desired multiband response with acceptable impedance matching across the targeted mid-band region. The objective of the second optimization is to further tune the key resonator dimensions for improved selectivity and out-of-band suppression over the desired 5G FR_1 band.

6.2. Optimized Dimensions and Design Tuning Rationale

Table 3 shows the optimized geometrical parameters obtained following the two optimization stages. The first optimization entailed design changes to achieve a multiband response, with the stub length set at 21 mm, and adjustment of SRR dimensions and coupling arrangement.

In the second stage, fine-tuning was made with different dimensions of resonators and stubs, which improved the control over the high-frequency spurious response and strengthened the out-of-band rejection. The remaining parameters, that is, ring width, split gap, and spacing between two rings, and feedline width thereof, were considered to remain constant in order to keep the coupling intact and maintain compatibility with practical fabrication. The changes made altered the effective LC resonance in the SRR cells and the frequency-dependent shunt loading introduced by the stub and DGS, hence increasing selectivity and thereby a cleaner stopband response in the optimized design.

6.3. Response after 1st Optimization

Figure 5 shows the simulated response for the 1st optimization. The filter exhibits strong frequency-selective behaviour with multiple resonant features and wideband matching behaviour. Impedance matching is better than -10dB over a broader region, starting from 1.17GHz up to 8.80GHz.

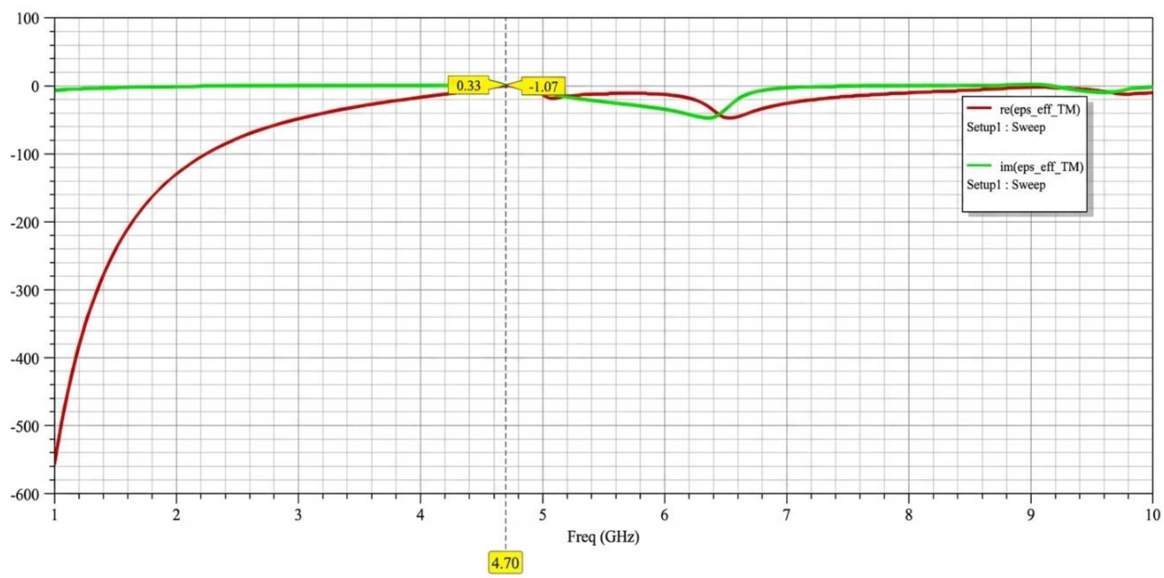

Fig. 2 Effective permittivity of the proposed SRR unit cell

Table 2. Dimensions of the proposed BPF

Parameter	Value (mm)	Parameter	Value (mm)
L_s: Substrate Length	32.0	g: Split Gap of SRR	0.9
W_s: Substrate Width	17.0	s: Spacing between SRR	0.9
W_f: Feed Line Width	2.0	w: Ring Width of SRR	1.1
L_{in}: Input Feed Length	4.0	W_d: DGS Slot Width (Top Bar)	15.0
L_{out}: Output Feed Length	4.0	L_d: DGS Slot Length	24.0
L/a: Outer Length of SRR	4.0	G_d: DGS Slot Width	2.0

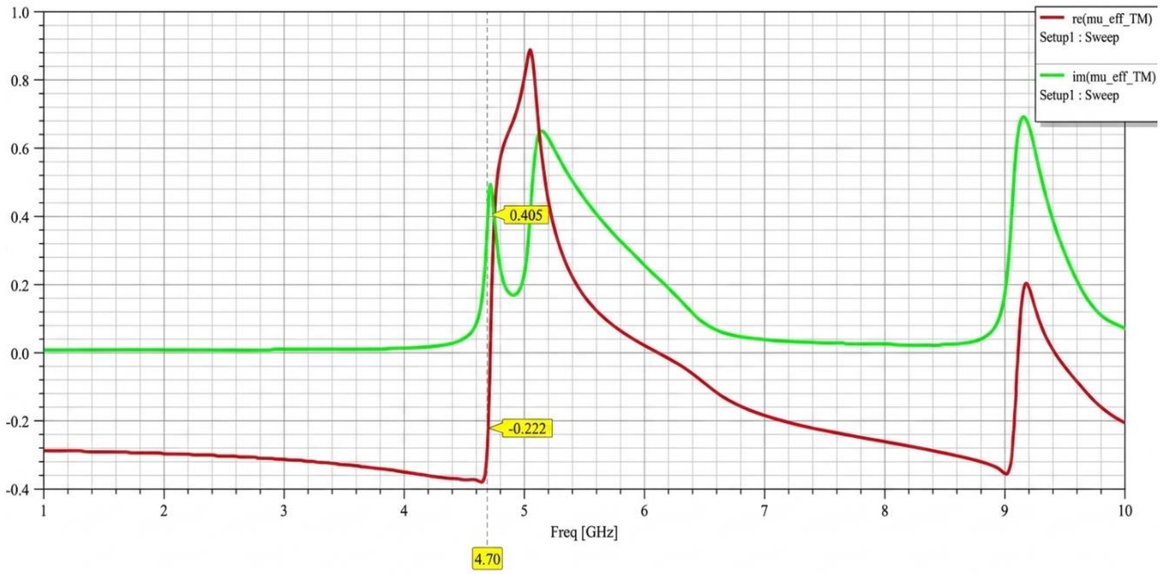

Fig. 3 Effective permeability of the proposed SRR unit cell

Table 3. Dimensions of the proposed BPF after 1st and 2nd optimization

Parameter	Value (mm) after 1st Optimization	Value (mm) after 2nd Optimization
Outer Length of SRR	3.2	3.0
Ring Width of SRR	1.0	0.7
Split Gap of SRR	0.7	0.5
Spacing between SRR	0.7	0.5

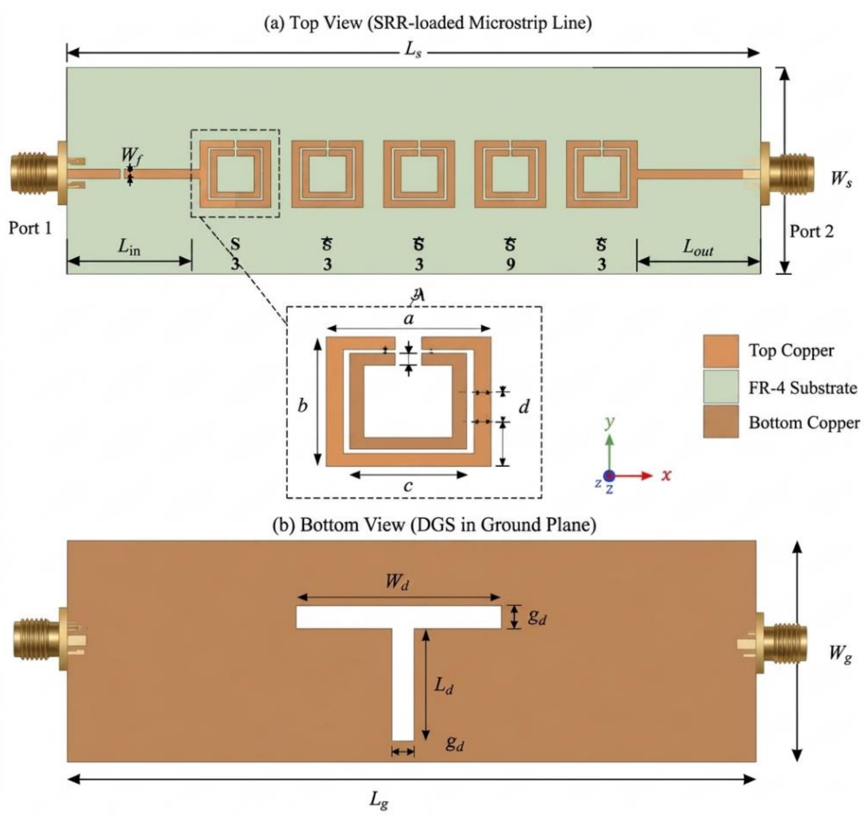

Fig. 4 Proposed BPF with I/O ports

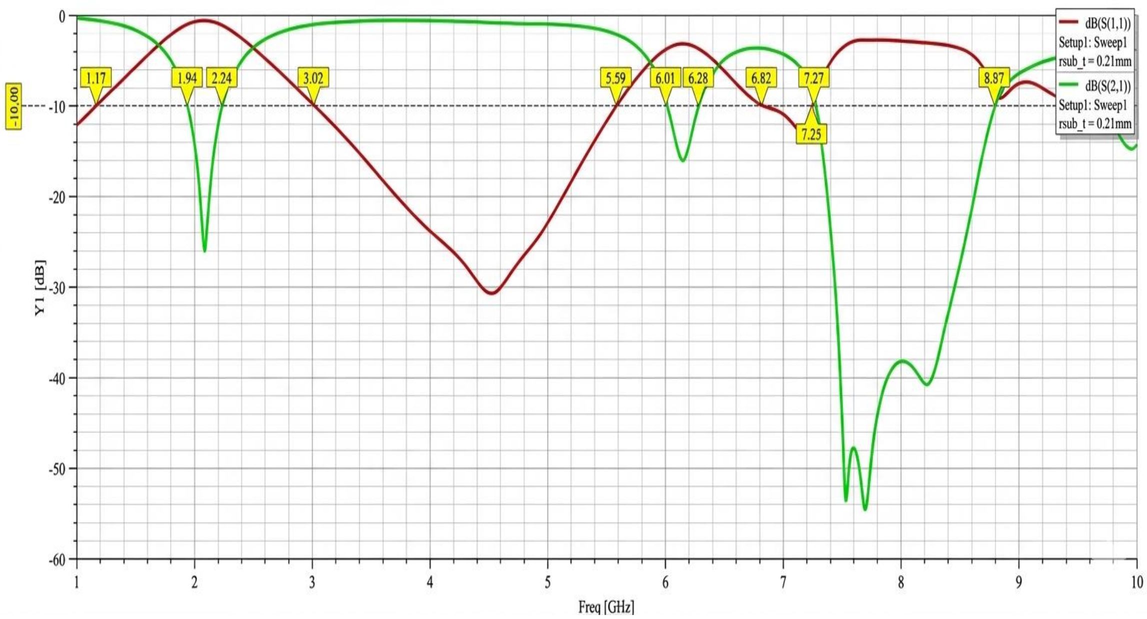

c

Fig. 5 Frequency response of the proposed BPF after 1st optimization

Transmission response also shows multiple characteristic points, resonant features around 1.94-2.24GHz, 6.01-6.28GHz, and 6.82-7.27GHz, showing the presence of multiple interacting resonances caused by the SRR array and ground perturbation. A wide matching range shows that the initial design gives a good port matching in a large frequency range, however it poses resonant interactions for the higher frequencies, which can cause undesirable resonant actions, and a second step is required to control the way that the transmission zeros are placed and to enhance the stopband beyond that required in the midband of 5G.

6.4. Response After 2nd Optimization

Figure 6 indicates the simulation results after the 2nd optimization. A strong resonance is achieved within the mid-band region for 5G, with the return loss reaching. $S_{11} \approx -36.56$ dB at 4.70 GHz. This supports the view of an excellent impedance match at the desired operating point. Further, the return loss remained below -10 dB around 3.30 GHz $S_{11} \approx -10.95$ dB, supporting the lower mid-band operation relevant to n77 and n78.

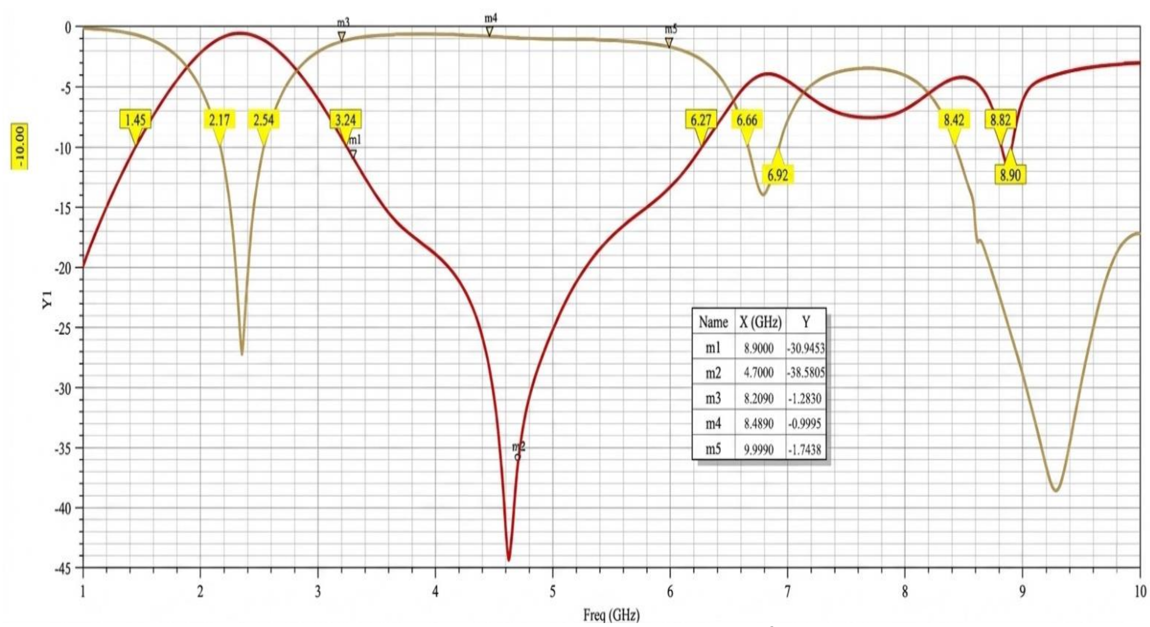

Fig. 6 Frequency response of the proposed BPF after 2nd optimization

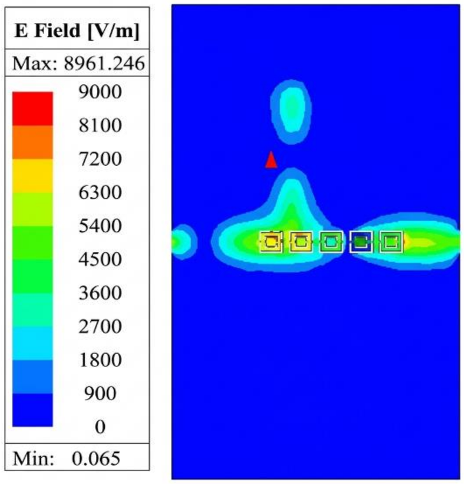

(a) Electric field analysis

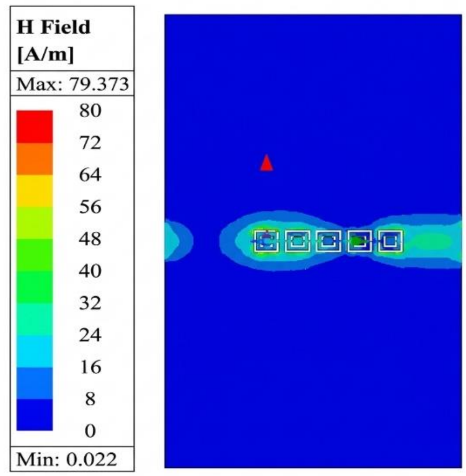

(b) Magnetic field analysis

Fig. 7 Electromagnetic field analysis of the proposed BPF

The transmission curve indicates that the system has to operate with minimal loss within its specified passband, yet exhibits significant signal attenuation at elevated frequencies due to its selective rejection of undesired signals.

The second optimization yields a more regulated response, exhibiting a distinct, strong resonance at 4.7 GHz and enhanced attenuation at elevated frequencies. The lowering of SRR ring length and stub length enhances performance by altering the equivalent LC resonances, so displacing unwanted higher-order modes from the working bands and reinforcing transmission zeros associated with the DGS.

The SRR array, through its design development process, establishes passband control, while the DGS and stub tuning mechanism mitigate stopband interference and diminish spurious signals. The system exhibits effective matching performance at 3.30 GHz, facilitating the operation of the lower mid-band regions of n77 and n78, while the 4.70 GHz deep resonance within n79 (4.4-5.0 GHz) enhances matching capability.

The suggested SRR-DGS topology operates efficiently for multiband 5G FR1 filtering applications within the n77, n78, and n79 frequency bands

6.5. Field Distribution Analysis to Verify SRR Excitation and Stopband Mechanism

The study utilized HFSS software to analyze electromagnetic field patterns, thereby validating that the SRR-DGS BPF design functions as intended in accordance with its defined operating concept. The electric field magnitude depicted in Figure 7(a) demonstrates significant localization along the split gaps and inner margins of the SRR cells, affirming the predominance of capacitive energy storage in the resonators and substantiating their LC characteristics. The maximum electric-field intensity attains roughly 8.96 kV/m, indicating robust resonator excitation at the designated operating frequency.

Figure 7(b) illustrates that the magnetic-field distribution predominantly occurs around the boundaries of the SRR loop, indicating that currents traverse these pathways while demonstrating magnetic resonance characteristics, with a peak magnetic field strength of 79.37 A/m.

The 3D model illustrates that the electric and magnetic fields are exclusively detected in proximity to the cascaded SRR chain. Passband formation occurs via unit cells, as numerous neighboring SRRs generate resonator interactions that facilitate multiband functionality and enhanced selectivity.

The T-shaped DGS operates as a high-frequency component suppressor by interacting with ground return currents to produce transmission zeros that enhance stopband rejection.

6.6. Fabrication, Measurement and Comparison of Simulated and Measured Results

The SRR-DGS multiband BPF is fabricated using a FR-4 substrate having a dielectric constant of 4.4 and a height of 1.6 mm. Figure 8 displays the fabricated prototype, which shows both the top SRR array section and the bottom T-shaped DGS section. The measurement system was connected to the filter through SMA connectors, which were soldered at the input and output microstrip ports. The Anritsu MS46122B Vector Network Analyzer (VNA) is used for scattering parameter measurements across a frequency range that extends from 1 GHz to 10 GHz. A 2 -port calibration at the RF cable endpoints to reduce all systematic errors while using an IF bandwidth of about 1 kHz to conduct measurements. The prototype results were measured as shown in Figure 9. The observed return loss (S_{11}) for the n77 and n78 region (3.3-4.2 GHz) continues in the ~ -12 to -20 dB range, showing acceptable impedance matching in the lower mid-band. The observed transmission S_{21} across the same range is close to 0 dB, which confirms that the structure operates as a passband with low attenuation and consequently can support n77 and n78 operation. As we get towards the upper mid-band, the filter resonates strongly in the n79 band, with the measured S_{11} at -22 to -25 dB at ~4.7 GHz, showing good matching, and the dominant resonance is in the desired n79 band. The measured S_{21} over this mid-band region remained near 0 dB, further indicating successful transmission in the proposed 5G FR_1 spectrum.

Most interestingly, a deep stopband region appears on the upper frequency range where the transmission drops to about -30 to -35 dB at ~8.4-8.6 GHz, followed by a prolonged attenuation towards the higher end of the sweep with further dips around ~ 9-9.5 GHz. The deep attenuation valleys demonstrate that the suggested SRR-DGS combination can successfully suppress spurious transmission at higher frequencies, which is in accordance with the T-shaped DGS's intended function to generate transmission zeros and clean the upper stopband. The observed features show the SRR array produces mid-band transmission over n77, n78 and n79, while the T-shaped DGS facilitates suppression of spurious higher frequency components and enhancement of stopband response.

The simulated and measured scattering properties of the constructed SRR-DGS BPF are presented in Figure 10. The simulated responses are represented as S_{11} (blue) and S_{21} (orange). The measured responses are plotted as S_{11} (cyan) and S_{21} (green). In general, the measured response follows the same pattern as the simulation, which confirms that the planned filtering mechanism is intact after fabrication on FR-4. The simulated return loss shows a deep resonance of about $S_{11} \approx -45$ dB around 4.7 GHz in the mid-band region, while the measured return loss at the same resonance shows about $S_{11} \approx -20$ to -25 dB, confirming good practical matching with the expected reduced depth due to fabrication tolerances and connector parasitic. Transmission-wise, the simulated and measured S_{21} are close to 0 dB in the primary passband region. The estimated insertion loss is around ~0.5-1.2 dB at the mid-band resonance, which is consistent with the FR-4 dielectric and conductor losses and the impacts of the SMA connectors.

The comparative plot of Figure. 10 further shows the appearance of different attenuation features formed by the combined SRR chain and the T-shaped DGS. A notable decline of attenuation is seen near 6.7-6.9 GHz, with transmission dropping down to about S21 ≈ -10 to -15 dB, both simulated and measured, showing efficient suppression of an unwanted spectral area.

The proposed filter also exhibits good stopband rejection at higher frequencies. The simulated response shows a deep attenuation valley of about S21 ≈ -35 to -40 dB around 9.1-9.3 GHz. The measured response shows a similar deep attenuation of about S21 ≈ -30 to -35 dB in the ~8.4–8.6 GHz domain, with continued suppression over much of the 8-10 GHz range. The measured curves show more ripple than the simulation, especially for the S21 at higher frequencies. This ripple is mainly caused by SMA soldering discontinuities, finite VNA dynamic range and FR-4 material dispersion, with frequency.

The comprehensive results indicate that the SRR unit-cell array attains mid-band resonance with negligible energy dissipation across its specified frequency range, but the DGS-assisted configuration produces significant upper band attenuation alongside improved stopband efficacy.

All frequency deviations and amplitude inconsistencies between simulation findings and measurement data correspond to the actual effects of FR-4 tolerances, SRR gap manufacture faults, and connection parasitic elements, which preserve the filtering characteristics demonstrated by the proposed BPF.

It can be observed from Table 4 that the SRR array + T-shaped DGS filter proposed in this paper surpasses the other embodiments provided in terms of obtaining a multiband response for 5G-FR1 networks at low cost on FR-4 with low insertion loss (~ 0.5-1.2 dB) at the mid-band on a high stopband (~ -30 to -35 dB), which seems to be very much in favor of this trade-off of cost, performance and implementation with the aim of making the 5G front compact.

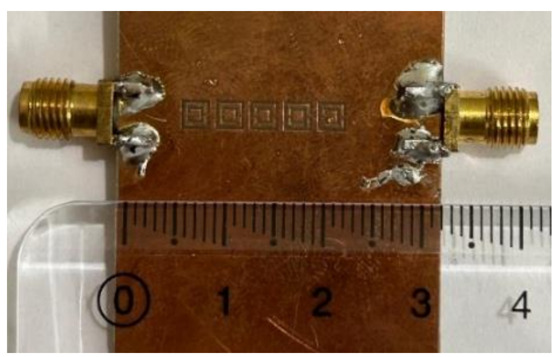

(a) Top view of the fabricated BPF

(b) Bottom view of the fabricated BPF

Fig. 8 Fabricated prototype of the BPF

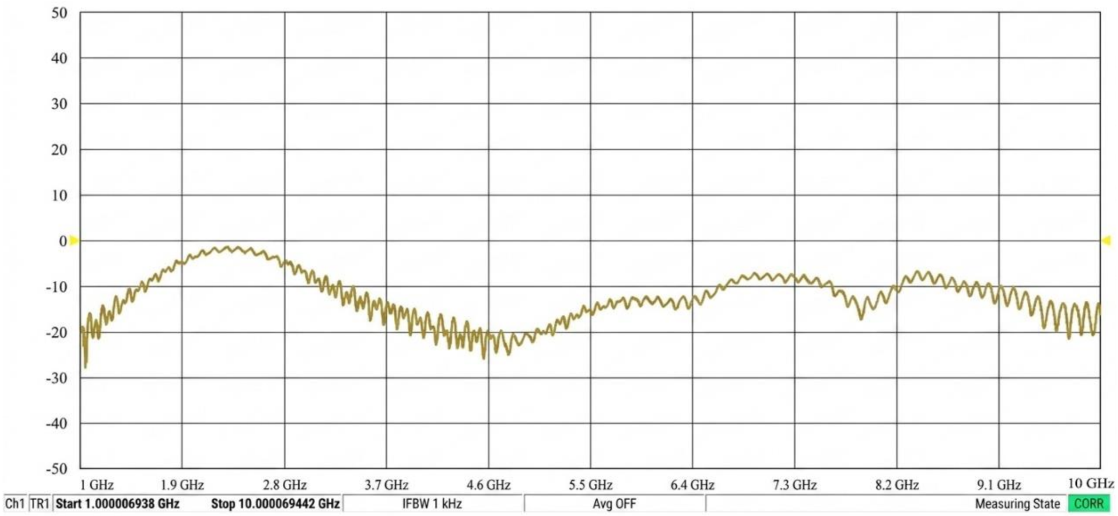

(a) Measured S_{11} on Anritsu MS46122B VNA

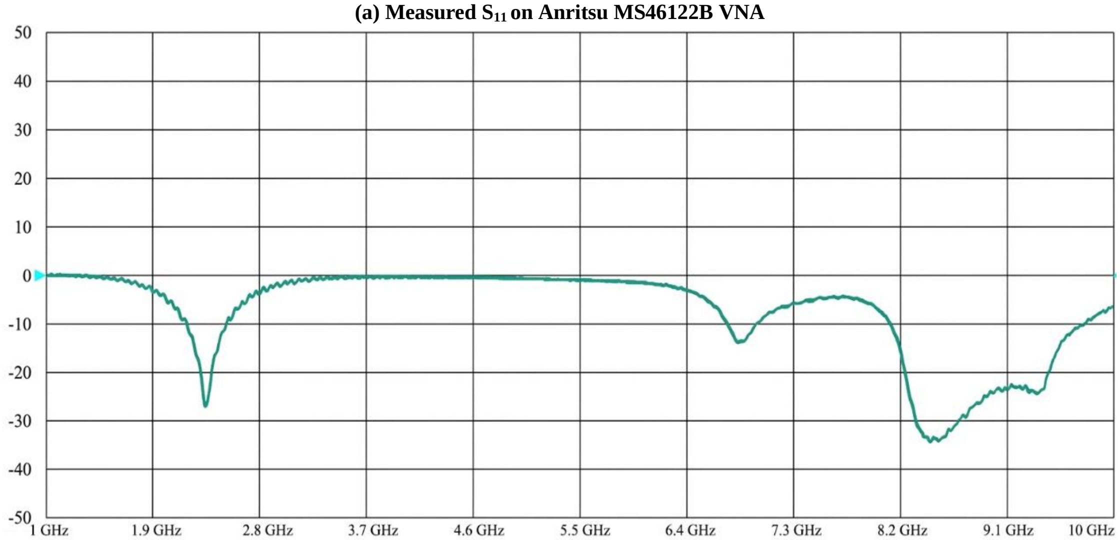

(b) Measured S_{21} on Anritsu MS46122B VNA

Fig. 9 Measured results of the fabricated prototype of the BPF

Table 4. Comparative evaluation with existing literature

Ref.	f_0 (GHz)	Technology	Material	IL (dB)	RL (dB)	FBW	Size
[8]	20.0	Cavity Resonators		0.3	17.0	1%	110x22x20 mm^3
[13]	14.2	Cavity Resonators		0.5	17.0	1%	18x18x12 mm^3
[16]	3.5	SAW/BAW	AlN	3.0	18.0	5%	3x5 mm^2
[21]	10.2	SIPW	Roger 5880	1.5	10.0	30%	36x18 mm^2
[22]	8.7	SIPW	FR-4	2.0	10.0	32%	34x12 mm^2
[25]	1.0	Planar	Roger 4003	2.5	15.0	1%	30x20 mm^2
[29]	2.4	SRR/CSRR	Roger 6010	2.5	16.0	5%	25x19 mm^2
[30]	1.0	SRR/CSRR	FR-4	1.5	16.0	20%	30x18 mm^2
[31]	9.0	SRR/CSRR	Roger 5880	3.8	15.0	1%	25x22 mm^2
[32]	5.0 8.9	SRR/CSRR	Roger 4003	6.2 5.2	12.0 18.0	6% 3%	20x24 mm^2
[33]	2.4	SRR/CSRR	Roger 6010	1.3	19.0	5%	26x26 mm^2
[35]	3.6	SRR/CSRR	Roger 5880	1.9	16.0	5%	27x18 mm^2
Present Work	4.7	Microstrip SRR unit-cell array + T-shaped DGS	FR-4	0.5-1.0	22.0-25.0	18%	32x17 mm^2

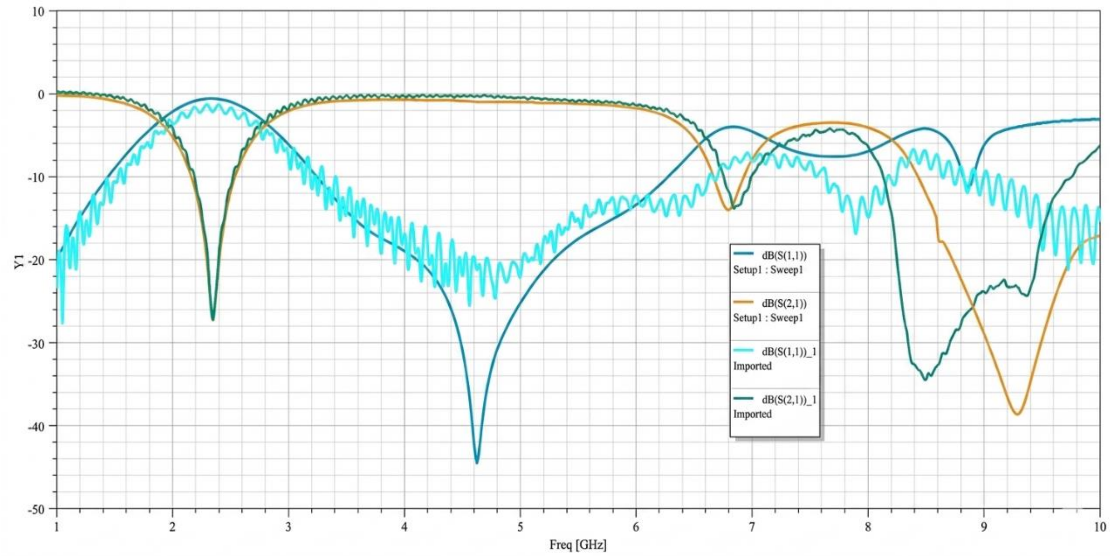

Fig. 10 Comparison between the simulated and measured results of the BPF

7. Conclusion and Future Scope

This paper presented an experimentally validated SRR unit-cell driven multiband microstrip bandpass filter for 5G FR1 operation covering n77, n78, and n79. The proposed topology combines a cascaded SRR array on the top layer with a T-shaped DGS in the ground plane. Unit-cell characterization through effective-parameter extraction verified resonance behavior consistent with SRR magnetic response near the design frequency, supporting the metamaterial-inspired interpretation of the structure.

The complete filter was designed and optimized in Ansys HFSS, fabricated on an FR-4 substrate, and measured using an Anritsu VNA. The measured S11 and S21 curves follow the simulated trend, confirming that the SRR chain establishes the intended mid-band transmission characteristics while the DGS assists in suppressing spurious high-frequency components and improving stopband cleanliness. Overall, the proposed SRR–DGS configuration provides a low-profile and fabrication-friendly solution for compact multiband filtering in sub-6 GHz 5G RF front-end modules. Several extensions can further strengthen the proposed platform. First, the filter can be redesigned on low-loss substrates and re-optimized using frequency-dependent material models to reduce insertion loss and improve simulation-measurement alignment.

Second, advanced ground-plane engineering, such as hybrid DGS patterns, multi-slot DGS, or CSRR-assisted ground defects, can be investigated to generate additional transmission zeros and further improve upper-stopband attenuation without increasing footprint.

Third, the SRR array can be generalized to non-uniform or multi-sized unit-cell distributions to better control multiband pole placement and suppress higher-order modes more effectively.

Fourth, robustness studies can be added, including tolerance analysis for SRR gap/spacing and SMA launch parasitics, enabling a more production-ready design.

Finally, integrating the filter into a representative 5G RF module environment would provide a system-level validation of performance under realistic packaging and interconnect conditions.

References

[1] Jiajia Wang et al., "Bandpass Filter for 5G Sub-6 GHz Bands," *Progress in Electromagnetics Research Letters*, vol. 116, pp. 79-85, 2024. [CrossRef] [Google Scholar] [Publisher Link]

[2] Gabriel Giribaldi et al., "Compact and Wideband Nanoacoustic Pass-Band Filters for Future 5G and 6G Cellular Radios," *Nature Communications*, vol. 15, no. 1, pp. 1-13, 2024. [CrossRef] [Google Scholar] [Publisher Link]

[3] Mouhssine Elbathaoui et al., "A Compact UWB Bandpass Filter based on Metamaterials for Sub-6 GHz 5 G and cmWave Band 6 G Wireless Communications," *Franklin Open*, vol. 13, pp. 1-12, 2025. [CrossRef] [Google Scholar] [Publisher Link]

[4] Monica Martinez-Mendoza et al., "Design of a Triband Lumped Element Filter for Digital Microwave Power Amplifiers," *2015 European Microwave Conference (EuMC)*, Paris, France, pp. 805-808, 2015. [CrossRef] [Google Scholar] [Publisher Link]

[5] Matthew A. Morgan, and Tod A. Boyd, "Theoretical and Experimental Study of a New Class of Reflectionless Filter," *IEEE Transactions on Microwave Theory and Techniques*, vol. 59, no. 5, pp. 1214-1221, 2011. [CrossRef] [Google Scholar] [Publisher Link]

[6] Muhammad Ali et al., "Miniaturized High-Performance Filters for 5G Small-Cell Applications," *2018 IEEE 68th Electronic Components and Technology Conference*, San Diego, CA, USA, pp. 1068-1075, 2018. [CrossRef] [Google Scholar] [Publisher Link]

[7] Muhammad Ali et al., "First Demonstration of Compact, Ultra-Thin Low-Pass and Bandpass Filters for 5G Small-Cell Applications," *IEEE Microwave and Wireless Components Letters*, vol. 28, no. 12, pp. 1110-1112, 2018. [CrossRef] [Google Scholar] [Publisher Link]

[8] Bahram Yassini, Ming Yu, and Brian Keats, "A *Ka*-Band Fully Tunable Cavity Filter," *IEEE Transactions on Microwave Theory and Techniques*, vol. 60, no. 12, pp. 4002-4012, 2012. [CrossRef] [Google Scholar] [Publisher Link]

[9] Bahram Yassini, and Ming Yu, "A Novel ka Band Dual Mode Super Q Cavity Filter," *2014 IEEE MTT-S International Microwave Symposium (IMS2014)*, Tampa, FL, USA, pp. 1-3, 2014. [CrossRef] [Google Scholar] [Publisher Link]

[10] Bahram Yassini, and Ming Yu, "Ka-Band Dual-Mode Super *Q* Filters and Multiplexers," *IEEE Transactions on Microwave Theory and Techniques*, vol. 63, no. 10, pp. 3391-3397, 2015. [CrossRef] [Google Scholar] [Publisher Link]

[11] Hai Hu, Ke-Li Wu, and Richard J. Cameron, "Stepped Circular Waveguide Dual-Mode Filters for Broadband Contiguous Multiplexers," *IEEE Transactions on Microwave Theory and Techniques*, vol. 61, no. 1, pp. 139-145, 2013. [CrossRef] [Google Scholar] [Publisher Link]

[12] Trong-Hieu Le et al., "A Novel Diplexer Integrated with a Shielding Case using High *Q* -Factor Hybrid Resonator Bandpass Filters," *IEEE Microwave and Wireless Components Letters*, vol. 28, no. 3, pp. 215-217, 2018. [CrossRef] [Google Scholar] [Publisher Link]

[13] Michal Baranowski et al., "The Design of Cavity Resonators and Microwave Filters Applying Shape Deformation Techniques," *IEEE Transactions on Microwave Theory and Techniques*, vol. 71, no. 7, pp. 3065-3074, 2023. [CrossRef] [Google Scholar] [Publisher Link]

[14] Hualei wang et al., "Design of Ladder-Type Saw/Baw Filters with Constant Group Delay," *2011 IEEE International Ultrasonics Symposium*, Orlando, FL, USA, pp. 345-348, 2011. [CrossRef] [Google Scholar] [Publisher Link]

[15] Dimitra Psychogiou, Roberto Gómez-García, and Dimitrios Peroulis, "SAW-based Bandpass Filters with Flat in-Band Group Delay and Enhanced Fractional Bandwidth," *2017 IEEE MTT-S International Microwave Workshop Series on Advanced Materials and Processes for RF and THz Applications (IMWS-AMP)*, Pavia, Italy, pp. 1-3, 2017. [CrossRef] [Google Scholar] [Publisher Link]

[16] Xian-Hu Zha et al., "Surface and Bulk Acoustic Wave Resonators based on Aluminum Nitride for Bandpass Filters," *AAPPS Bulletin*, vol. 34, no. 1, pp. 1-15, 2024. [CrossRef] [Google Scholar] [Publisher Link]

[17] Pu Chen, Guangxi Li, and Zhiyuan Zhu, "Development and Application of SAW Filter," *Micromachines*, vol. 13, no. 5, pp. 1-15, 2022. [CrossRef] [Google Scholar] [Publisher Link]

[18] Yasir I.A. Al-Yasir et al., "Recent Progress in the Design of 4G/5G Reconfigurable Filters," *Electronics*, vol. 8, no. 1, pp. 1-17, 2019. [CrossRef] [Google Scholar] [Publisher Link]

[19] Kai Yang et al., "Advanced RF Filters for Wireless Communications," *Chip*, vol. 2, no. 4, pp. 1-26, 2023. [CrossRef] [Google Scholar] [Publisher Link]

[20] Gabriel Giribaldi et al., "Compact and Wideband Nanoacoustic Pass-Band Filters for Future 5G and 6G Cellular Radios," *Nature Communications*, vol. 15, no. 1, pp. 1-13, 2024. [CrossRef] [Google Scholar] [Publisher Link]

[21] Longfang Ye et al., "Substrate Integrated Plasmonic Waveguide for Microwave Bandpass Filter Applications," *IEEE Access*, vol. 7, pp. 75957-75964, 2019. [CrossRef] [Google Scholar] [Publisher Link]

[22] Yuxuan Luo et al., "A Compact Microwave Bandpass Filter based on Spoof Surface Plasmon Polariton and Substrate Integrated Plasmonic Waveguide Structures," *Applied Physics A*, vol. 128, no. 2, 2022. [CrossRef] [Google Scholar] [Publisher Link]

[23] Gaurav Mittal, and Nagendra Prasad Pathak, "Spoof Surface Plasmon Polaritons based Microwave Bandpass Filter," *Microwave and Optical Technology Letters*, vol. 63, no. 1, pp. 51-57, 2021. [CrossRef] [Google Scholar] [Publisher Link]

[24] Asad Aziz, "A Novel Plasmonic Waveguide for Extraordinary Field Enhancement of Spoof Surface Plasmon Polaritons with Low-Loss Feature," *Results in Optics*, vol. 5, pp. 1-9, 2021. [CrossRef] [Google Scholar] [Publisher Link]

[25] Chih-Jung Chen, "Design of Parallel-Coupled Dual-Mode Resonator Bandpass Filters," *IEEE Transactions on Components, Packaging and Manufacturing Technology*, vol. 6, no. 10, pp. 1542-1548, 2016. [CrossRef] [Google Scholar] [Publisher Link]

[26] Faroq Razzaz, Saud M. Saeed, and Majeed A.S. Alkanhal, "Ultra-Wideband Bandpass Filters using Tapered Resonators," *Applied Sciences*, vol. 12, no. 7, pp. 1-12, 2022. [CrossRef] [Google Scholar] [Publisher Link]

[27] Li Yang et al., "Novel Multilayered Ultra-Broadband Bandpass Filters on High-Impedance Slotline Resonators," *IEEE Transactions on Microwave Theory and Techniques*, vol. 67, no. 1, pp. 129-139, 2019. [CrossRef] [Google Scholar] [Publisher Link]

[28] A.J. Salim et al., "A Polygonal Open-Loop Resonator Compact Bandpass Filter for Bluetooth and WLAN Applications," *IOP Conference Series: Materials Science and Engineering*, vol. 433, no. 1, pp. 1-9, 2018. [CrossRef] [Google Scholar] [Publisher Link]

[29] Mohamad Syahral, and Achmad Munir, "Development of Multiple Elements of SRR-based Bandpass Filter," *2016 10th International Conference on Telecommunication Systems Services and Applications (TSSA)*, Denpasar, Indonesia, pp. 1-4, 2016. [CrossRef] [Google Scholar] [Publisher Link]

[30] Zaid A. Abdul Hassain, Amer Abbood AL-Behadili, and Adham R. Azeez, "First Order Parallel Coupled BPF with Wideband Rejection based on SRR and CSRR," *Telkomnika (Telecommunication Computing Electronics and Control)*, vol. 17, no. 6, pp. 2704-2712, 2019. [CrossRef] [Google Scholar] [Publisher Link]

[31] Ria Lovina Defitri, and Achmad Munir, "X-Band Microstrip Narrowband BPF Composed of Split Ring Resonator," *2016 Progress in Electromagnetic Research Symposium (PIERS)*, Shanghai, China, pp. 3468-3471, 2016. [CrossRef] [Google Scholar] [Publisher Link]

[32] Mohammed Berka et al., "Dual-Band Bandpass Filter based on Electromagnetic Coupling of Twin Square Metamaterial Resonators (SRRs) and Complementary Resonator (CSRR) for Wireless Communications," *Journal of Electronic Materials*, vol. 50, no. 8, pp. 4887-4895, 2021. [CrossRef] [Google Scholar] [Publisher Link]

[33] Zenal Aripin et al., "Compact SRR-based Microstrip BPF for Wireless Communication," *2015 2nd International Conference on Information Technology, Computer, and Electrical Engineering (ICITACEE)*, Semarang, Indonesia, pp. 474-477, 2015. [CrossRef] [Google Scholar] [Publisher Link]

[34] Mohamed Hesham, and Sameh O. Abdellatif, "Compact Bandpass Filter based on Split Ring Resonators," *2019 International Conference on Innovative Trends in Computer Engineering (ITCE)*, Aswan, Egypt, pp. 301-303, 2019. [CrossRef] [Google Scholar] [Publisher Link]

[35] Chi-Hyung Ahn, Dong-Jin Jung, and Kai Chang, "Compact Parallel-Coupled Line Bandpass Filter using Double Complementary Split Ring Resonators," *Microwave and Optical Technology Letters*, vol. 55, no. 3, pp. 506-509, 2013. [CrossRef] [Google Scholar] [Publisher Link]

[36] Monish Gupta, and Jyoti Saxena, "Microstrip Filter Designing by SRR Metamaterial," *Wireless Personal Communications*, vol. 71, no. 4, pp. 3011-3022, 2013. [CrossRef] [Google Scholar] [Publisher Link]

[37] K.V. Vineetha, M. Siva Kumar, and B.T.P. Madhav, "Analysis of Triple Band Split Ring Resonator based Microstrip Bandpass Filter," *Journal of Physics: Conference Series*, vol. 1804, no. 1, pp. 1-6, 2021. [CrossRef] [Google Scholar] [Publisher Link]

[38] Jonathan Carver, Vianney Reignault, and Frédérique Gadot, "Engineering of the Metamaterial-based Cut-Band Filter," *Applied Physics A*, vol. 117, no. 2, pp. 513-516, 2014. [CrossRef] [Google Scholar] [Publisher Link]

[39] Seif Naoui, Lassaad Latrach, and Ali Gharsallah, "Equivalent Circuit Model of Double Split Ring Resonators," *International Journal of Microwave and Optical Technology*, vol. 11, no. 1, pp. 1-6, 2016. [Google Scholar] [Publisher Link]

[40] Edward J. Rothwell et al., "Analysis of the Nicolson-Ross-Weir Method for Characterizing the Electromagnetic Properties of Engineered Materials," *Progress in Electromagnetics Research*, vol. 157, pp. 31-47, 2016. [CrossRef] [Google Scholar] [Publisher Link]